

2. Krätschmer, W., Fostiropoulos, K. & Huffman, D. R. *Chem. Phys. Lett.* **170**, 167–170 (1990).
3. Krätschmer, W., Lamb, L. D., Fostiropoulos, K. & Huffman, D. R. *Nature* **347**, 354–358 (1990).
4. Bethune, D. S., Johnson, R. D., Salem, J. R., de Vries, M. S. & Yannoni, C. S. *Nature* **366**, 123–128 (1993).
5. Saito, Y., Yoshikawa, T., Fujimoto, N. & Shinohara, H. *Phys. Rev. B* **48**, 9182–9185 (1993).
6. Armbruster, J. F. et al. *Phys. Rev. B* (submitted).
7. Shinohara, H. et al. *J. phys. Chem.* **97**, 4259–4261 (1993).
8. Kikuchi, K. et al. *Chem. Phys. Lett.* **216**, 67–91 (1993).
9. Dorn, H. C. et al. *Analyt. Chem.* (in the press).
10. Stevenson, S. et al. *Analyt. Chem.* (in the press).
11. Wang, X. et al. *J. appl. Phys.* **32**, L866–L868 (1993).
12. Van Tendeloo, G. & Amelinckx, S. *Adv. Mater.* **5**, 620–629 (1993).
13. Muto, S. et al. *Phil. Mag. B* **67**, 443–463 (1993).
14. Kikuchi, K. et al. *Chem. Lett.* **16**, 1607–1610 (1991).
15. Diederich, F. & Whetten, R. L. *Accts. Chem. Res.* **25**, 119–126 (1992).
16. Kikuchi, K. *Nature* **357**, 142–145 (1992).
17. Manolopoulos, D. E., Fowler, P. W., Taylor, R., Kroto, H. W. & Walton, D. J. *chem. Soc., Faraday Trans.* **88**, 3117–3118 (1992).
18. Zhang, X. W. & Ho, D. S. *Phys. Rev. Lett.* **69**, 69–72 (1992).
19. Raghavachari, K. *Chem. Phys. Lett.* **190**, 397–400 (1992).
20. Wang, B. L. & Ho, D. S. *J. chem. Phys.* **96**, 7183–7185 (1992).
21. Bakioes, D. et al. *Chem. Phys. Lett.* **200**, 411–417 (1992).
22. Schneider, U., Richard, S., Kappes, M. M. & Ahlrichs, R. *Chem. Phys. Lett.* **210**, 165–169 (1993).
23. Manolopoulos, D. E. & Fowler, P. W. *J. chem. Phys.* **96**, 7603–7614 (1992).
24. Yannoni, C., Bernier, P., Bethune, D., Meijer, G. & Salem, J. *J. Am. chem. Soc.* **113**, 3190–3192 (1991).
25. Fleming, R. et al. in *Proc. Mater. Res. Soc. Vol. 206* (eds Averback, R. S., Berhole, J. & Nelson, D. L.) 691–696 (Materials Research Soc., Pittsburgh, 1991).

ACKNOWLEDGEMENTS. We thank D. Dorn and L. Jackson for technical assistance, and acknowledge financial support from the Virginia Center for Innovative Technology. C.H.K. acknowledges support from the US NSF and the Materials and Molecular Simulation Center (supported by DOE-AICD, Allied-Signal, BP America, Asahi Chemical, Asahi Glass, Chevron, BF Goodrich and Xerox).

Biological magnetic resonance imaging using laser-polarized ^{129}Xe

M. S. Albert*, G. D. Cates†, B. Driehuys†,
W. Happer†, B. Saam†, C. S. Springer Jr*
& A. Wishnia**‡

* Department of Chemistry, State University of New York, Stony Brook, New York 11794-3400, USA

† Department of Physics, Princeton University, Princeton, New Jersey 08544, USA

As currently implemented, magnetic resonance imaging (MRI) relies on the protons of water molecules in tissue to provide the NMR signal. Protons are, however, notoriously difficult to image in some biological environments of interest, notably the lungs¹ and lipid bilayer membranes such as those in the brain². Here we show that ^{129}Xe gas can be used for high-resolution MRI when the nuclear-spin polarization of the atoms is increased by laser optical pumping and spin exchange^{3–6}. This process produces hyperpolarized ^{129}Xe , in which the magnetization is enhanced by a factor of about 10^5 . By introducing hyperpolarized ^{129}Xe into mouse lungs we have obtained images of the lung gas space with a speed and a resolution better than those available from proton MRI^{1,7} or emission tomography^{8,9}. As xenon (a safe general anaesthetic) is rapidly and safely transferred from the lungs to blood and thence to other tissues^{8,9}, where it is concentrated in lipid^{10–15} and protein^{13,15–18} components, images of the circulatory system, the brain and other vital organs can also be obtained. Because the magnetic behaviour of ^{129}Xe is very sensitive to its environment, and is different from that of $^1\text{H}_2\text{O}$, MRI using hyperpolarized ^{129}Xe should involve distinct and sensitive mechanisms for tissue contrast.

The magnetic resonance signal strength of a given nuclear species depends on its total magnetization in the chosen sample volume element; that is, on the product of the species concentration, the excess spin density per nucleus (polarization), and the volume of the element. In the largest available magnetic fields, thermal-equilibrium polarizations reach $\sim 10^{-5}$, which is

adequate for $^1\text{H}_2\text{O}$ imaging. Other proton species, and all other nuclear species, have concentrations too small to be of use in conventional high-speed, high-resolution MRI. Xenon gas at 1 atm, for example, has a molar concentration only 0.04% that of tissue $^1\text{H}_2\text{O}$. However, the polarization of ^{129}Xe and other spin 1/2 noble gases can be enormously enhanced through spin-exchange with an optically pumped alkali metal vapour^{3–5}. In our case, a dilute vapour of rubidium (~ 1 p.p.m. of the Xe pressure) is kept spin-polarized by the absorption of 1–2 W of circularly polarized 795-nm Rb D₁-resonance light from a Ti:sapphire laser. Gas-phase collisions between the ^{129}Xe and the polarized Rb atoms result in the transfer of angular momentum from the Rb valence electron to the ^{129}Xe nucleus. The ^{129}Xe gas is laser-polarized to at least 25% in 5–20 min (depending on conditions), enhancing its NMR signal to $\sim 10^5$ times the thermal equilibrium value. The gas is then delivered for imaging.

Figure 1a–c shows the evolution in time (0–10 s) of the distribution of hyperpolarized ^{129}Xe entering the lungs of a mouse lung-heart preparation. In Fig. 1a the xenon has just begun to enter the lungs. In Fig. 1b the lungs are so inflated that they press against the interior of the 10-mm diameter glass tube in which they are contained. Finally, in Fig. 1c the lungs have started to deflate and the two lobes are clearly visible. The bright spot toward the centre is a cross-section of the trachea through which the xenon was introduced. All three ^{129}Xe images are dark in the region between the lung lobes where the heart is located. Comparison with a standard $^1\text{H}_2\text{O}$ image (Fig. 1d), in which the heart is prominent and the lungs invisible, illustrates one aspect of the complementary nature of proton- and ^{129}Xe -MRI. All ^{129}Xe images in Fig. 1 were obtained in 600 ms at an average lung Xe concentration of ~ 20 mM (1.2×10^{19} atoms cm^{-3}), which is tiny compared to the 80–100 M proton concentrations typical of $^1\text{H}_2\text{O}$ imaging; yet the signal intensities, spatial resolution ($0.14\text{–}0.28\text{ mm}^3$), and data acquisition rates all exceed those obtained in standard clinical $^1\text{H}_2\text{O}$ -MRI. Moreover, the magnetization densities are so large that several images can be generated in rapid succession, allowing for real-time tracking of physiological processes.

The large and long-lived ^{129}Xe magnetization densities achieved in the lung provide a basis for imaging beyond the lung itself—MRI of ^{129}Xe transported from the lung to various tissues is feasible. To assess the MRI parameters for ^{129}Xe in lipid environments we imaged a tube of octanol, a standard cell-membrane model, containing dissolved (205 mM) thermally-polarized xenon. The images were of lower resolution (20 mm^3) and required 7 min to obtain but clearly demonstrate the feasibility of using ^{129}Xe to image tissue. With hyperpolarized ^{129}Xe , high-resolution images comparable to those of Fig. 1 could be obtained in a single rapid imaging scan, even for the lower concentrations expected in tissue. In the brain, for example, a xenon concentration of ~ 10 mM is expected for a subject breathing 50% xenon¹⁵.

Imaging with a hyperpolarized species depends on the transport of sufficient surviving magnetization to tissues of interest. The polarization decays with the longitudinal relaxation time T_1 , which must be long in the lungs and blood. We have measured $T_1 \sim 30$ s for gaseous ^{129}Xe in the excised mouse lungs. Adjusting for the O₂-relaxivity¹⁹ in a normally breathing subject we project values of 12–15 s in the lung. We also obtained a T_1 value of ~ 40 s for ^{129}Xe dissolved in partly deoxygenated rat blood. We estimate T_1 for ^{129}Xe in fully-oxygenated cell membranes to be >15 s (refs 15, 20, 21). This estimate must be compared to the time it takes for xenon to reach various tissues. Inhaled xenon reaches equilibrium with the entire blood volume in one blood circuit, (~ 1 s in a mouse, and ~ 15 s in a human^{9,22,23}). As transport and relaxation times are of the same order of magnitude, one can expect significant accumulation of highly polarized ^{129}Xe in all tissues.

The importance of this technique hinges on the radically

‡ To whom correspondence should be addressed.

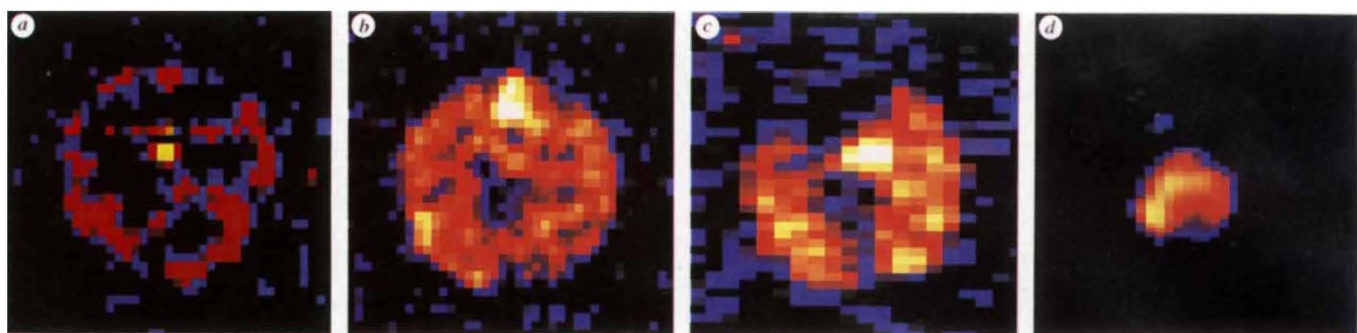
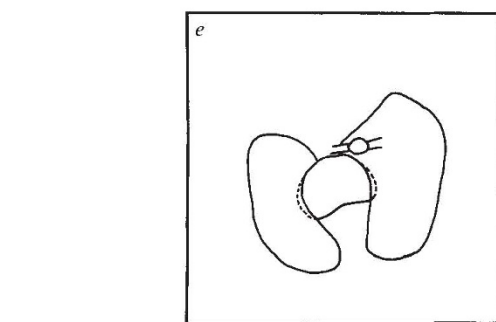


FIG. 1 Magnetic resonance images of the excised lungs and heart of a mouse as laser-polarized ^{129}Xe enters the lungs through the trachea: ^{129}Xe images, (a–c); $^1\text{H}_2\text{O}$ image, (d). All images are nominally of the same 1-mm-thick axial slice (perpendicular to the axis of the vertebral column), adjusted to the same scale: the lung outline in (a–c) is 10 mm in diameter. *a*, About 1 s after seal-breakage, *in situ* N_2 is still being displaced, and ^{129}Xe delivery is in progress. Probably only the larger air vessels are seen. Pixel resolution is $0.37 \text{ mm} \times 0.37 \text{ mm}$, image recorded in 600 ms. *b*, A second heart-lung preparation ~2 s after seal breakage. Gas mixing in the fully-inflated lungs is complete. *c*, The same preparation 7 s later, imaged with the remaining ^{129}Xe hypermagnetization. The lungs are relaxed. Pixel size here is $0.37 \text{ mm} \times 0.74 \text{ mm}$, imaging time 300 ms. *d*, ^1H image of the same preparation. The bright heart fills the dark region of *c*. Note the absence of signal from lung-tissue $^1\text{H}_2\text{O}$, typical behaviour of regions with ultra-short T_2 when subjected to standard MRI. (Non-standard MRI can extract low-contrast signal from lung water, but images take 20–40 min (refs 1, 7) to acquire.) *e*, Diagram of the axial section of the preparation, corresponding to *c* and *d*, sketching the positions of the trachea, lung lobes, and heart.

METHODS. 3 atm of xenon gas, enriched to 70% ^{129}Xe , was laser-polarized as reported⁵, in glass cells containing a few mg Rb metal, and Rb vapour at $\sim 2 \times 10^{12} \text{ atoms cm}^{-3}$. After 20 min of irradiation the cell is seated in the delivery system. The polarized ^{129}Xe is transferred when a break-seal on the cell is ruptured with a piston. The Rb vapour cools,

different magnetic and physiological properties of ^{129}Xe and $^1\text{H}_2\text{O}$. In $^1\text{H}_2\text{O}$ -MRI, the small range of contrast arising from variations in local $^1\text{H}_2\text{O}$ concentration (proton-density contrast) is enhanced by exploiting the ~3-fold variation of the longitudinal (T_1) and transverse (T_2) nuclear spin-relaxation times within normal and pathological tissues^{24,25}. The T_1 and T_2 variations for ^{129}Xe in lipid membranes, water, and proteins are much larger and more sensitive to chemical environment^{15,20,21}, particularly to O_2 concentration²¹. This broad range of ^{129}Xe T_1 and particularly of T_2 values should make it possible to distinguish between different tissue types. Further, the 20 p.p.m. range in resonance frequency of ^{129}Xe among the various tissue components^{14,15,18}, ~200 p.p.m. away from the gas-phase resonance, may permit differential imaging of these components. In contrast, the resonance frequency of $^1\text{H}_2\text{O}$ in tissue is essentially invariant. Lastly, the hyperpolarized ^{129}Xe density in a tissue depends markedly on xenon transport. Changes in blood flow induced by physiological activity should produce straightforward changes in local hyperpolarized ^{129}Xe density contrast.

MRI with hyperpolarized ^{129}Xe already appears quite promising in comparison with other advanced imaging techniques. In lung imaging, for example, the only serious alternative to ^{129}Xe MRI is high-resolution X-ray computed tomography (HRCT). Typical resolutions of 4 mm^3 are obtained in 2 s but with a heavy radiation dose (1–5 rem) to the subject²⁶. With ^{129}Xe MRI one could obtain HRCT-like images of lung tissue density variation, using the gas-phase ^{129}Xe resonance, but one could also obtain images of the time-dependent dissolving ^{129}Xe distribution that reflects alveolar function. ^{129}Xe signal strength sufficient to image 4-mm^3 volume elements in a 0.6 s MRI FLASH scan would be obtained if 40 ml of pure 25% polarized ^{129}Xe (150 ml of natural Xe) were inhaled into the lung. Routine



condenses and is adsorbed onto the surfaces of the delivery system during transfer. Images were obtained using a Bruker MSL 400 instrument operating at 110.7 MHz for ^{129}Xe , with an 89 mm bore, 9.4 T vertical magnet and high-gradient Bruker microimaging probe. All images were obtained with a single Fast-Low-Angle-Shot (FLASH^{30,31}) sequence and the same maximum encoding field gradients (resulting in a field of view of $47 \text{ mm} \times 47 \text{ mm}$ for the ^{129}Xe images, and $13 \text{ mm} \times 13 \text{ mm}$ for ^1H), using either 128×128 (a, b) or 64×128 matrices (c, d).

production of such quantities is currently practical. The low cost of Xe gas (~\$15–20 per litre in bulk for natural-abundance Xe) will permit imaging at higher resolution of lung and of other tissues, which requires inhalation of larger volumes of hyperpolarized ^{129}Xe . If desired, Xe, which is not metabolized, can readily be recovered from the exhaled gas. Like standard $^1\text{H}_2\text{O}$ imaging, ^{129}Xe MRI should be a safe procedure.

Thus laser-polarized ^{129}Xe has the potential to add significantly to the scope of MRI. We note that ^3He is also an attractive candidate for imaging; it can be produced with comparable hyperpolarization, and has a larger magnetic moment and longer relaxation times²⁷. The prospect of scaling-up hyperpolarized noble-gas technology to human subjects, and all tissues, is promising. Although this extension will require larger quantities of hyperpolarized ^{129}Xe than those used in a mouse, the much larger volume elements ordinarily imaged will tolerate lower concentrations. A single commercially available Ti:sapphire laser system can in principle produce about 1 g h^{-1} of highly polarized ^{129}Xe (ref. 28), which can be stored frozen for hundreds of hours without substantial loss of polarization²⁹. We believe the way is open to ^{129}Xe imaging of any desired portion of a living mammal. □

Received 7 February; accepted 7 June 1994.

- Bergin, C. J., Pauly, J. M. & Macovski, A. *Radiology* **179**, 777–781 (1991).
- Bárány, M. et al. *Magn. Reson. Imaging* **5**, 393–398 (1987).
- Bhaskar, N. D., Happer, W. & McClelland, T. *Phys. Rev. Lett.* **49**, 25–28 (1982).
- Happer, W. et al. *Phys. Rev. A29*, 3092–3110 (1984).
- Cates, G. D. et al. *Phys. Rev. A45*, 4631–4639 (1992).
- Raftery, D. et al. *Phys. Rev. Lett.* **66**, 584–587 (1991).
- Gewalt, S. L. et al. *Magn. Reson. Med.* **29**, 99–106 (1993).
- Susskind, H. et al. *Prog. nucl. Med.* **5**, 144–170 (1978).
- Susskind, H., Ellis, K. J., Atkins, H. L., Cohn, S. H. & Richards, P. *Prog. nucl. Med.* **5**, 13–34 (1978).
- Pollack, G. L., Himm, J. F. & Enyeart, J. *J. J. chem. Phys.* **81**, 3239–3246 (1984).

11. Wilcock, R. J., Battino, R., Danforth, W. F. & Wilhelm, E. *J. chem. Thermodynam.* **10**, 817–822 (1978).
12. Wilhelm, E., Battino, R. & Wilcock, R. *J. Chem. Rev.* **77**, 219–243 (1977).
13. Wishnia, A. *Biochemistry* **8**, 5064–5070 (1969).
14. Miller, K. W. et al. *Proc. natn. Acad. Sci. U.S.A.* **78**, 4946–4949 (1981).
15. Albert, M. S., Springer, C. S., Murphy, R. & Wishnia, A. *Abstr. 11th A. Mtg Soc. magn. Reson. Med.* (ed. Wehrli, F. W.) 2104 (SMRM, Berkeley, California, 1992).
16. Wishnia, A. *Biochemistry* **8**, 5070–5075 (1969).
17. Schoenborn, B. P. *J. molec. Biol.* **45**, 297–303 (1969).
18. Tilton, R. F. Jr & Kuntz, I. D. *Jr Biochemistry* **21**, 6850–6857 (1982).
19. Jameson, C. J., Jameson, A. K. & Hwang, J. K. *J. chem. Phys.* **89**, 4074–4081 (1988).
20. Diehl, P. & Jokisaari, J. *J. mag. Reson.* **88**, 660–665 (1990).
21. Albert, M. S., Springer, C. S. & Wishnia, A. *Abstr. 11th A. Mtg Soc. magn. Reson. Med.* (ed. Wehrli, F. W.) 4710 (SMRM, Berkeley, California, 1992).
22. Blumgart, H. L. & Weiss, S. *J. clin. Invest.* **4**, 339–411, 423–425 (1927).
23. Knudsen, G. M., Pettigrew, K. D., Patlak, C. S. & Paulson, O. B. *Am. J. Physiol.* (in the press).
24. Fullerton, G. D. & Cameron, I. L. In *Biomedical Magnetic Resonance Imaging* (eds Wehrli, F. W., Shaw, D. & Kneeland, J. B.) 147 (VCH, New York, 1988).
25. Ogawa, S. et al. *Proc. natn. Acad. Sci. U.S.A.* **89**, 5951–5955 (1992).
26. Mayo, J. R. et al. *Radiology* **163**, 507–510 (1987).
27. Newbury, N. R., Barton, A. S., Cates, G. D., Happer, W. & Middleton, H. *Phys. Rev. A* **48**, 4411–4420 (1993).
28. Cates, G. D. et al. *Phys. Rev. Lett.* **65**, 2591–2594 (1990).
29. Gatzke, M. et al. *Phys. Rev. Lett.* **70**, 690–693 (1993).
30. Haase, A., Frahm, J., Matthaei, D., Haenische, W. & Merboldt, K. D. *J. mag. Reson.* **67**, 258–266 (1986).
31. Albert, M. S., Huang, W., Lee, J.-H., Patlak, C. S. & Springer, C. S. *Jr Magn. Reson. Med.* **29**, 700–714 (1993).

ACKNOWLEDGEMENTS We thank V. Avona for the gift of Xe gas enriched to 70% ^{129}Xe (obtained from Isotech Inc. Miamisburg, Ohio). We also thank F. Bonner for use of his vacuum system, and D. Harrington for providing some optical components. M.S.A. thanks D. Balamore for introducing him to this subject and for discussions, and also thanks Y. Xu for discussions. This work was supported in part by grants from the AFOSR (G.D.C.), the US NIH (C.S.S.) and the US NSF (A.W. and M.S.A.).

Radiocarbon evidence for a smaller oceanic carbon dioxide sink than previously believed

Vago Hessheimer*, Martin Heimann† & Ingeborg Levin*

* Institut für Umweltphysik, University of Heidelberg,
Im Neuenheimer Feld 366, D-69120 Heidelberg, Germany
† Max-Planck-Institut für Meteorologie, Bundesstrasse 55,
D-20146 Hamburg, Germany

RADIOCARBON produced naturally in the upper atmosphere or artificially during nuclear weapons testing is the main tracer used to validate models of oceanic carbon cycling, in particular the exchange of carbon dioxide with the atmosphere^{1–3} and the mixing parameters within the ocean itself^{4–7}. Here we test the overall consistency of exchange fluxes between all relevant compartments in a simple model of the global carbon cycle, using measurements of the long-term tropospheric CO₂ concentration⁸ and radiocarbon composition^{9–12}, the bomb ^{14}C inventory in the stratosphere^{13,14} and a compilation of bomb detonation dates and strengths¹⁵. We find that to balance the budget, we must invoke an extra source to account for 25% of the generally accepted uptake of bomb ^{14}C by the oceans³. The strength of this source decreases from 1970 onwards, with a characteristic timescale similar to that of the ocean uptake. Significant radiocarbon transport from the remote high stratosphere and significantly reduced uptake of bomb ^{14}C by the biosphere can both be ruled out by observational constraints. We therefore conclude that the global oceanic bomb ^{14}C inventory should be revised downwards. A smaller oceanic bomb ^{14}C inventory also implies a smaller oceanic radiocarbon penetration depth¹⁶, which in turn implies that the oceans take up 25% less anthropogenic CO₂ than had previously been believed.

The atmospheric $^{14}\text{CO}_2$ activity has undergone large excursions since the beginning of nuclear bomb tests (Fig. 1a and b, solid lines). After the Test Ban treaty in 1962 the bomb ^{14}C signal in the atmosphere is declining because of $^{14}\text{CO}_2$ exchange with the ocean and the other carbon reservoirs. The behaviour of these ^{14}C exchange fluxes over time depends mainly on the total carbon fluxes between the reservoirs, and on the internal circulation dynamics within these reservoirs.

The temporal variation of the tropospheric radiocarbon inventory N_{trop} is determined by the net exchange fluxes with the ocean F_O , the terrestrial biosphere F_B , and the stratosphere F_S , by input from anthropogenic sources Q_{Trop} , and the radioactive decay (^{14}C has a mean lifetime $\lambda^{-1} = 8,275 \text{ yr}$) as follows

$$d(N_{\text{trop}})/dt = F_O + F_B + F_S + Q_{\text{Trop}} - \lambda N_{\text{trop}}$$

Only the global response on the interannual timescale to a major atmospheric perturbation is examined in this study. We can therefore use relatively simple models to determine the respective radiocarbon fluxes. For the ocean, a type of robust Oeschger and Siegenthaler box diffusion model^{4,5} was adopted using a vertical eddy diffusion coefficient $K = 7,685 \text{ m}^2 \text{ yr}^{-1}$ coupled to 7.8 yr residence time of atmospheric CO₂ with respect to air/sea gas exchange. The flux F_O , calculated according to our tropospheric boundary conditions, matches the integrated oceanic bomb ^{14}C uptake (until 1 January 1974) of 300×10^{26} atoms (Fig. 2a) derived from oceanic measurements during GEOSECS³, and compares well with results of the most recent version of the HILDA¹⁷ ocean model.

The model biosphere is divided into three boxes where the input carbon is decomposed exponentially with an e-folding constant given by the turnover time τ . Box 1 has a mass of 105 Gt-C (gigatonnes carbon; 1 Gt = 10^{15} g), $\tau = 3 \text{ yr}$, and accounts for fine roots, twigs and leaves. Box 2 has a mass of 675 Gt-C, $\tau = 27 \text{ yr}$, and represents big roots, stems and branches. Boxes 1 and 2 couple directly to the troposphere, and the sum of their input fluxes, determining the net primary productivity, is set to 60 Gt-C yr^{-1} . Box 3, the 'old carbon reservoir' has a mass of 1,420 Gt-C and $\tau = 375 \text{ yr}$. Box 3 contains the slowly decomposing material of boxes 1 and 2, gets its carbon input equally distributed from these boxes, and is needed to account for the low $\Delta^{14}\text{C}$ values measured in soil organic carbon¹⁸. These settings correspond to previously published estimates for the terrestrial biosphere¹⁹. We did not account for fertilisation and destruction fluxes when calculating F_B from the tropospheric boundary conditions.

Our model stratosphere consists of one box with the same CO₂ concentration as the model troposphere, and a turnover time of 2.5 yr with respect to the troposphere. The total mass of the stratosphere box corresponds to 15% of the total atmospheric air mass. F_S was calculated from the bomb input scenario and the measured tropospheric boundary conditions.

The initial conditions in 1945 for all reservoirs were computed starting at preindustrial equilibrium in AD 1750 (atmospheric concentrations: 280 p.p.m.v. CO₂, $\Delta^{14}\text{C} = -4.5\text{\textperthousand}$). Using observed atmospheric CO₂ concentrations⁸ and $^{14}\text{CO}_2$ data^{9,12} (Fig. 3b) as prescribed input data in all scenarios, we automatically account for the dilution of $^{14}\text{CO}_2$ by input of ^{14}C free carbon from fossil fuel consumption (Suess effect²⁰). All natural ^{14}C production ($P_{\text{nat}} = 2.3 \times 10^{26}$ atoms yr^{-1} , assumed to be constant) occurred in the stratosphere.

The anthropogenic input of $^{14}\text{CO}_2$ by the nuclear industry, contributing significantly to the tropospheric inventory only from about 1970 onwards, was calculated for different reactor types using the normalized $^{14}\text{CO}_2$ emission data per generated electrical energy reported by Bonka²¹ and in UNSCEAR²². The latter was estimated for the period of 1970 to 1990 from the installed plants worldwide, assuming a capacity utilization of 60% for all reactor types. $^{14}\text{CO}_2$ emissions from reprocessing plants were also taken from UNSCEAR²². The $^{14}\text{CO}_2$ release from the nuclear industry in 1990 was estimated to be less than 0.5×10^{26} ^{14}C -atoms yr^{-1} , increasing almost linearly from 1970 onwards (compare Fig. 2b).

^{14}C input from the atmospheric bomb tests was estimated based on the compilation of bomb strength data¹⁵ (Fig. 1b), and, depending on the respective scenario, adjusting the specific ^{14}C production per megatonne (Mt) TNT to the tropospheric and stratospheric observations during the time period of the major ^{14}C rises. The uncertainty of this adjustment is small as